Main Manuscript for

Mechanism for kinetic polarity revealed by FtsZ from a cell wall-less bacterium *Spiroplasma*

Joyeeta Chakraborty[1], Sakshi Poddar[2,3], Soumyajit Dutta[1], Vaishnavi Bahulekar[1], Shrikant Harne[1], Ramanujam Srinivasan[2,3], Pananghat Gayathri[1*]

[1] Biology Division, Indian Institute of Science Education and Research, Pune – 411008, India

[2] School of Biological Sciences, National Institute of Science Education and Research,

Bhubaneswar – 752050, India

[3] Homi Bhabha National Institutes (HBNI), Training School Complex, Anushakti Nagar, Mumbai,

India 400094

*Pananghat Gayathri

Email: gayathri@iiserpune.ac.in

Competing Interest Statement: The authors declare no conflict of interest.

Classification: Biochemistry, Microbiology

Keywords: FtsZ, kinetic polarity, treadmilling, cell wall-less bacteria

Abstract

FtsZ, the tubulin homolog essential for bacterial cell division, assembles the Z-ring at the division site, and directs peptidoglycan synthesis by its treadmilling action. A key unanswered question is how FtsZ achieves its kinetic polarity that drives treadmilling. To obtain insights into fundamental features of FtsZ assembly dynamics independent of peptidoglycan synthesis, we report the characterization of FtsZ from the cell wall-less bacterium *Spiroplasma melliferum* (SmFtsZ). SmFtsZ was a slow GTPase and required higher critical concentration (CC) for polymerization as compared to *Escherichia coli* FtsZ (EcFtsZ). In FtsZs, a conformational switch from R- to T-state favors polymerization. In the crystal structures of SmFtsZ, conformation of the GTP-bound N-terminal domain (NTD) was in the T-state, while the relative orientation of the NTD and the C-terminal domain (CTD) matched the R-state. Hence, the crystal structures represent a conformational state that facilitates preferential binding of the NTD of the monomeric GTP-bound SmFtsZ to the CTD-exposed end of SmFtsZ filament. CTD of the nucleotide-bound monomer cannot bind to the NTD-exposed end of the filament unless relative rotation of the domains leads to cleft opening. The mutation F224M in SmFtsZ cleft resulted in higher GTPase activity and lower CC, whereas the corresponding M225F in EcFtsZ resulted in cell division defects in *E. coli*. These results suggest that relative rotation of the domains leading to cleft opening is a rate-limiting step of polymerization. This slows the addition of monomers to the NTD-exposed end of the filament in comparison to the CTD end, thus explaining kinetic polarity.

Introduction

FtsZ, a tubulin homolog, is one of the essential cytoskeletal proteins involved in bacterial cell division (1, 2). At the onset of division, FtsZ localizes at the mid-cell forming a ring-like structure known as Z-ring (3). The Z-ring tethers to the membrane via proteins like FtsA, an actin homolog, or ZipA and recruits other proteins required for cell division (4, 5). This results in the formation of a multiprotein complex called divisome that constricts the cell, eventually leading to two daughter cells (6). The precise mechanism of how ring constriction takes place and the role of FtsZ filament dynamics in the process is not fully understood. Earlier studies have characterized FtsZs from cell walled bacteria (7–9). Based on these studies, cell wall synthesis is thought to be the primary force generator for constriction and the rate-limiting process in cytokinesis or septum closure (10–14).

FtsZ has a conserved domain architecture similar to tubulin, consisting of a GTP-binding N-terminal domain (NTD) and a C-terminal domain (CTD) connected via H7 helix (15). FtsZ makes homopolymers comprising a single protofilament, in contrast to tubulin, which forms heteropolymers of alpha and beta tubulin making 13-stranded microtubule assembly (16, 17). FtsZ polymerization is a cooperative process that requires a critical concentration of monomers for filament assembly (18–21). In addition, FtsZ filaments exhibit treadmilling, as opposed to the typical dynamic instability observed in microtubules. A conformational switch of each monomer from its low affinity state (R-state; relaxed state favored by monomers) to a high affinity state (T-state; tense state adopted by monomers within a filament) favors cooperative assembly of FtsZ filaments (20, 22, 23). In the R-state, the inter-domain cleft between the NTD and the CTD is closed whereas in the T-state, it is open (23, 24). The transition from R- to T-state within a monomeric subunit is thermodynamically less favorable due to the requirement of a positive free energy for opening of the inter-domain cleft (25). However, within protofilaments, the interactions between adjacent subunits provide the required energy for opening the cleft and favors R- to T-state transitions to form a protofilament (25).

Another important feature of FtsZ filament dynamics is kinetic polarity, which is interestingly opposite to what is known for microtubules (26). Microtubules elongate

from the end at which the N- terminal domain of beta-tubulin is exposed (referred to as the top end hereafter), whereas FtsZ elongates from the end with an exposed C-terminal domain (referred to as the bottom end hereafter) (26, 27). However, the structural basis for the opposite directionality of polymerization for the two homologous proteins is unknown.

In this study, we characterized FtsZ from *Spiroplasma melliferum*, which is a cell wall-less bacterium (SmFtsZ), and compared it with the relatively characterized FtsZ from *Escherichia coli* (EcFtsZ), a cell walled bacterium. We chose SmFtsZ from the cell wall-less bacteria as a model to study fundamental features of FtsZ in ring constriction and cytokinesis, independent of cell wall synthesis.

Biochemical analysis of SmFtsZ revealed a lower GTPase activity and higher critical concentration of filament formation than EcFtsZ. Crystal structures showed the presence of a domain-swapped dimer in an intermediate state, in which the NTD is in the T-state orientation and CTD is in the R-state orientation. The crystal structures of SmFtsZ in different nucleotide states illustrated that the nucleotide orientation can transit from R- to T- state, independent of conformational changes in the CTD. GTP binding induced conformational changes in the T3 loop that triggers polymerization. We identified a residue (Phe224 in SmFtsZ) in the cleft between the N- and C-terminal domains, which determines the ease of transition from the R-state to the T-state. Our *in vitro* and *in vivo* characterization of the inter-domain cleft mutants of SmFtsZ and EcFtsZ support the relevance of the residue in driving the facile conversion to the T-state.

These observations led us to propose a structural basis for the kinetic polarity of FtsZ, where transition of the NTD to the T-state conformation driven by GTP binding is sufficient to add a GTP-bound monomer to the bottom interface of the FtsZ filament. Addition of subunit to the top interface of the filament requires an additional step of rotation of the CTD, and hence could be a rate limiting step after nucleotide binding. Based on the structures of FtsZ conformational states, biochemistry and *in vivo* experiments, we thus provide a mechanistic basis for kinetic polarity in polymerization of FtsZ filaments.

Results

SmFtsZ has higher critical concentration and lower GTPase activity than EcFtsZ *in vitro*

We purified SmFtsZ (**Figure S1A, B**) and performed sedimentation assay in order to find out the condition in which SmFtsZ forms filaments. SmFtsZ was observed in the pellet fraction specifically in the presence of GTP and not upon addition of GDP (**Figure 1A**). Further, observation of SmFtsZ filaments in presence of GTP and Mg^{2+} using electron microscopy (**Figure 1B**) led us to conclude that SmFtsZ formed filaments in the presence of GTP similar to other characterized bacterial FtsZs.

As the GTPase active site is at the interface between two monomers in the FtsZ filament (**Figure S1C**), GTP hydrolysis is expected to occur upon filament formation. Hence, we used rate of GTP hydrolysis as a proxy to estimate critical concentration (CC) of filament formation. An estimate of CC will approximately be the concentration above which k_{obs} (defined as the amount of GTP hydrolysis per unit concentration of the enzyme per unit time) reaches a constant value. For SmFtsZ, we estimated a CC of approximately 8 μM, above which an approximately constant activity of 0.63 ± 0.03 min^{-1} (k_{obs}; average of k_{obs} of the protein concentrations above estimated CC) was observed (**Figure 1C**), whereas for EcFtsZ a lower value of approximately 1 μM (**Figure 1D**) was observed for a constant k_{obs} of 1.78 ± 0.04 min^{-1} (average of k_{obs} of the protein concentrations above estimated CC). We then measured the specific activity of these two proteins at a saturating concentration of GTP, the GTP concentration being fixed based on the Michaelis-Menten plot (**Figure 1E, F**). The specific activities (k_{cat}) were estimated as 0.87 ± 0.02 min^{-1} and 1.51 ± 0.05 min^{-1} for SmFtsZ and EcFtsZ, respectively, consistent with the values above, suggesting an approximately two to three-fold lower activity for SmFtsZ (**Figure 1G**). Activity measurement of the active site mutant $SmFtsZ^{D211G}$ showed that the mutation abrogated the GTPase activity and $SmFtsZ^{\Delta CT}$, a truncated construct of SmFtsZ without the C-terminal flexible linker, showed similar

activity as the wild type (**Figure 1G**). Importantly, the Michaelis-Menten plot also revealed that the K_m of SmFtsZ (234 μM) was 7 times higher than that of EcFtsZ (34 μM) (**Table S1**). Hence, the catalytic efficiency for SmFtsZ is 12 times lower than that of EcFtsZ (**Table S1**). Thus, our biochemical data demonstrates that SmFtsZ requires a higher critical concentration for filament formation with a lower GTPase activity compared to EcFtsZ (**Tables S1, S2**) under similar *in vitro* conditions.

Crystal structures of SmFtsZ$^{\Delta CT}$ captured as domain swapped dimers

To obtain mechanistic insights on SmFtsZ activity, we crystallized SmFtsZ$^{\Delta CT}$ (a truncated construct of SmFtsZ without the C-terminal flexible linker; **Figure S1A**), without and with addition of GMPPNP (a non-hydrolyzable analog of GTP). SmFtsZ$^{\Delta CT}$ showed similar GTPase activity compared to the wild type (**Figure 1G**). Crystal structures of both GDP-bound SmFtsZ$^{\Delta CT}$ (GDP intrinsically bound to the protein during purification; **Figure S1D, E**) and GMPPNP-bound SmFtsZ$^{\Delta CT}$ (**Figure S1F**) were obtained in the same space group and unit cell, implying a similar crystal packing (**Table S3**). Interestingly, the two molecules in the asymmetric unit exist as a domain-swapped dimer (**Figure 2A**), wherein the NTD of one chain packed against the CTD of the other chain, together resembling the globular structure of FtsZ (**Figure 2A, B**). In the extended conformation of one molecule of the domain-swapped dimer (**Figure 2C**), the NTD and the CTD were separated at the T6 loop which is the start of the H7 helix. A clear and continuous electron density in the T6 loop region was observed in this region for chain A (**Figure 2D**), confirming the domain-swapped conformation of SmFtsZ$^{\Delta CT}$ in the crystal structure. For chain B, the corresponding loop was disordered and hence the residue stretch of 170–185 has not been modelled (**Figure 2D**). The relative orientations of the NTD and CTD in the extended conformation of each chain (A and B) are different (**Figure 2D**).

Despite the presence of a domain-swapped dimer in the crystal structure, the SEC-MALS profile indicates predominantly a monomeric nature for SmFtsZ$^{\Delta CT}$ in solution at

lower concentrations of the protein (**Figure 2E**). At a higher concentration, the SEC profile shows two peaks - a major peak corresponding to a monomer form and a minor peak corresponding to a dimeric form (**Figure 2F**). Since the polymerization interface is occluded in the domain-swapped conformation, the conformation cannot polymerize, which might have facilitated preferential crystallization of the domain-swapped dimer. Though no nucleotide was added during crystallization, GDP was found bound in the nucleotide pocket in both chains of one of the structures (PDB ID: 7YSZ) (**Figure S1D**). The bound GDP was likely to have been obtained from *E. coli* cells during expression and purification of SmFtsZ$^{\Delta CT}$ (seen in HPLC of denatured protein extract of purified protein, **Figure S1E**). In the second structure (PDB ID: 7YOP) where GMPPNP was added prior to crystallization, GDP and GMPPNP were observed in the nucleotide-binding pockets of chain A and chain B, respectively (**Figure S1F**).

SmFtsZ$^{\Delta CT}$ structures represent an intermediate conformation between R- and T-states

To further investigate the structural details of the unique conformations of SmFtsZ$^{\Delta CT}$, we compared the structures of GDP-bound R-state (PDB ID: 2RHL), GDP-bound T-state (PDB ID: 3VOA), and GTP-bound T-state (PDB ID: 3WGN) conformations of FtsZ, respectively. In the structures of chain A of PDB IDs 7YSZ and 7YOP, the orientation of the guanine ring of GDP matched with that of the R-state of FtsZ, while in chain B of both 7YSZ (GDP bound) and 7YOP (GMPPNP bound), the orientation of the nucleotide base corresponded to that of the T-state (**Figure 3A**). The angle between the plane of the guanine ring in the R- and T- states (**Figure 3B**) for all available crystal structures of FtsZ (**Table S4**) confirmed the conformational state of the nucleotide states as above.

As mentioned earlier, the domain-swapped dimers exist as two globular SmFtsZ molecules, with the NTD of one chain packed against the CTD of the other. Based on the comparison of the crystal structures of T- and R-states of other FtsZs, it is known that

NTD and CTD are in an open conformation in the T-state, while they are in the closed conformation in the R-state. To analyze the orientation of the CTD with respect to the NTD in the globular unit of SmFtsZ$^{\Delta CT}$, the NTD of the domain-swapped SmFtsZ$^{\Delta CT}$ structure and other FtsZ structures were superposed using PDB ID 3VOA as the reference structure. Subsequently, the RMSD between the CTDs of the reference structure with 70 FtsZ structures (**Table S4**) were calculated and plotted (**Figure 3C**). The plot revealed that the relative orientations of NTD and CTD of the globular domain-swapped SmFtsZ$^{\Delta CT}$ subunit resembled that of an R-state conformation (**Figure 3C**). Hence, from the above analyses, we concluded that in chain B the nucleotide-bound NTD is in T-state whereas the relative orientation between NTD and CTD corresponds to the R-state orientation. We refer to this unique conformational state that has not been observed before in any other structures of FtsZ as an intermediate state.

Gamma-phosphate of the nucleotide stabilizes the filament compatible conformation of the T3 loop

To analyze the conformational changes in the GMPPNP-bound state in comparison to the GDP-bound state, the NTD of GDP- (chain A and B of 7YSZ, chain A of 7YOP) and GMPPNP-bound (chain B of 7YOP) structures were superposed. A clear distinction was seen in the partial ordering of the T3 loop of SmFtsZ$^{\Delta CT}$, which surrounds the gamma phosphate and is also involved in interaction with the subunit above in the filament (**Figure S2A, B**) (28). We found that in the GDP-bound R-state (chain A, PDB ID: 7YSZ and 7YOP), the loop was ordered with the carbonyl group of Gly71 of T3 loop facing towards the nucleotide phosphates. A water mediated interaction between carbonyl oxygen of Gly71 and with the beta phosphate of GDP was observed in chain A of both the structures (**Figure 4A, B**). In the GDP bound T-state (chain B of 7YSZ), the loop was only partially modeled due to poor electron density. In the GMPPNP-bound state (chain B of 7YOP), the peptide of Gly71 of the loop was modeled in a flipped-out conformation, away from the nucleotide (**Figure 4C, D**), an essential change for accommodating the gamma phosphate without steric clash with the carbonyl oxygen of Gly71. The flipped

conformation of the peptide matches with that of the filament interacting conformation of T3 loop (as observed in 3WGN; **Figure S2C**). Based on these observations, we propose that the flipping of Gly71 and stabilization of the T3 loop is a trigger for GTP-induced polymerization of FtsZ (**Figure 4E**). The absence of an adjacent subunit that satisfies the contacts from a polymerization interface resulted in a partial disorder of the T3 loop of the two T-state conformations in chain B of 7YOP and 7YSZ, respectively.

Further, the conformation of Tyr145 from the T5 region was affected in accordance with the changes in the T3 loop, indicating a cross talk between T3 and T5 in a T-state transition. A clear density for Tyr145 was observed in the GDP-bound R-states (chain A) (**Figure 4A, B**). However, in the GDP- and GMPPNP-bound T-state structures (chain B of 7YSZ and 7YOP respectively), a strong difference density corresponding to an alternative conformation of Tyr145, which pointed towards the conserved Pro74 of the T3 loop was observed. In the absence of stabilizing interactions from the adjacent filament subunit, the alternate position of the Tyr145 was incompatible with the ordered conformation of the T3 loop (**Figure 4C, D**).

A flexible residue in the inter-domain cleft facilitates state transition in FtsZ

Based on our biochemical characterization and observations from the crystal structure, SmFtsZ appeared to have a higher critical concentration and a tendency to form a domain-swapped dimer during crystallization, a state achieved probably during the transition from R- to T-state. A key step for the R-state to T-state transition, which determines the critical concentration and kinetics of polymerization, is the relative rotation between NTD and CTD leading to opening of the cleft between them. We identified the interacting residues across the cleft and analyzed their conservation across FtsZ sequences from different organisms (**Figure S3A**). A notable difference was the observation of phenylalanine (Phe224) in strand S7 of SmFtsZ, instead of methionine at the equivalent position in most other FtsZs (including EcFtsZ or *Staphylococcus aureus* FtsZ; SaFtsZ) (**Figure 5A**). The conformations of this residue in the R-state and T-state

for both the chains of SmFtsZ$^{\Delta CT}$ structures are shown (**Figure 5A insets**). We hypothesized that the relatively smaller size and greater flexibility of methionine in comparison to phenylalanine might facilitate the transition from one state to another (e.g., in EcFtsZ). This might result in the lower CC and higher GTPase activity of EcFtsZ in comparison to SmFtsZ.

To test our hypothesis, we mutated Phe224 to methionine in SmFtsZ$^{\Delta CT}$ (SmFtsZ$^{F224M\Delta CT}$), purified the mutant protein (**Figure S3B, C**) and performed biochemical assays. To find if the mutation confers any change in the process of nucleation (by comparison of critical concentrations), GTPase assay with different concentrations of SmFtsZ^{F224M} was performed. It was observed that the k_{obs} remained constant above a protein concentration of approximately 3 µM for SmFtsZ^{F224M} (**Figure 5B**). This indicated that the critical concentration of the mutant was lower than the wild type. We observed from the Michaelis-Menten plot (**Figure 5C**) that the catalytic efficiency of this mutant was four times higher (**Table S1**) and the GTPase activity was approximately three times higher than that of the wild type (**Figure 5D, Table S2**). Observation of filaments using electron microscopy in presence of GTP with and without pelleting showed that the average length of SmFtsZ^{F224M} filaments (**Figure 5E**) was higher than that of SmFtsZ (**Figure 1B**). We also obtained the structure of SmFtsZ$^{F224M\Delta CT}$ in presence of GDP (PDB ID: 8GRW, **Table S3**) but the protein could not be crystalized with GMPPNP, probably due to efficient filament formation. Although the GDP-bound SmFtsZ$^{F224M\ \Delta CT}$ structure was a domain-swapped dimer similar to that of the wild type structure (**Figure S3D**), the methionine at position 224 interacted with fewer residues as compared to that of phenylalanine in wild type SmFtsZ (**Figure 5A inset**). Thus, based on the CC and the GTPase activity measurements, the cleft mutant, SmFtsZ^{F224M}, demonstrated that a smaller and more flexible residue at position 224 (residue numbering as in SmFtsZ) in the inter-domain cleft might be important for a quicker transition from R- to T-state.

A rigid phenylalanine instead of flexible methionine in the inter-domain cleft in EcFtsZ affects *E. coli* cell division

EcFtsZ and many other bacterial FtsZs have a methionine at the position equivalent to SmFtsZ-Phe224. We, hence, sought to test if a phenylalanine at this position in EcFtsZ would affect FtsZ function *in vivo*. To test if EcFtsZ^{M225F} affects cell division in absence of EcFtsZ, we utilized the *E. coli* strain JKD7-1 carrying the plasmid pKD3 (29). In this strain, the chromosomal *ftsZ* gene is disrupted by a kanamycin cassette. EcFtsZ is expressed from the plasmid pKD3, which is temperature sensitive for replication due to the *repAts* allele. Thus, the growth of this strain is permissible only at 30 ºC as the plasmid ceases to replicate at higher temperatures, resulting in the loss of *ftsZ*. However, at 42 ºC, growth can be achieved only upon supplementing FtsZ from an additional plasmid such as pJSB100, wherein FtsZ is expressed from an arabinose inducible promoter. Thereby, only EcFtsZ or only mutants of FtsZ that can support division in the absence of FtsZ^{WT} would give rise to viable colonies on plates containing arabinose at 42 ºC.

We therefore first tested, using spotting assay, if EcFtsZ^{M225F} mutant supported growth of JKD7-1 strain at 42 ºC, i.e., in the absence of any endogenous EcFtsZ protein. EcFtsZ served as the positive control and the empty vector pJSB2 as the negative control. While all of them grew well at 30 ºC in the presence of 1% glucose (added as a repressor to prevent any expression from the arabinose promoter, pBAD, in pJSB2 derived plasmids), no colony formation was observed with the vector alone (pJSB2) at 42 ºC as expected. Both EcFtsZ and EcFtsZ^{M225F} formed colonies on plates with 0.2 % arabinose under the restrictive temperature of 42 ºC and permissive temperature of 30 ºC, which also expressed the wild type FtsZ through the pKD3 plasmid (**Figure 6A**). However, a microscopic examination of the EcFtsZ^{M225F} mutant at the restrictive temperature of 42 ºC in liquid cultures revealed aberrant cell division with many filamentous cells (**Figure 6B**), indicating that the mutant was not fully functional. An analysis of their cell lengths showed that the cells expressing EcFtsZ^{M225F} exhibited filamentous morphology and were much longer than those expressing EcFtsZ. The average cell lengths of the wildtype and

M225F mutant were found to be 4.58 µm ± 0.09 (number of cells counted were at least 218, N = 3) and 12.45 µm ± 4.47 (number of cells counted were at least 100, N = 3) respectively (**Figure 6C**).

These results suggested that although EcFtsZ^{M225F} mutant supported colony formation, the mutation affected cell division in *E. coli* as observed from the filamentous phenotype of the cells.

Imperfect ring assembly accompanies defective cell division

We next sought to assess the effect of expression of EcFtsZ^{M225F} mutant on FtsZ ring assembly. In particular, we hypothesized that if the change to phenylalanine slowed down the state of transition, the ectopic expression of EcFtsZ^{M225F} in *E. coli* cells carrying the chromosomal copy of FtsZ, might affect the cell growth and FtsZ ring assembly. In order to monitor FtsZ ring assembly, we utilized a strain BW27783, wherein the wildtype chromosomally encoded FtsZ is fluorescently tagged (FtsZ$^{55-56}$-SW-mNeonGreen) and is functional (30). We expressed untagged version of either EcFtsZ or EcFtsZ^{M225F} from the arabinose inducible promoter of pJSB2 derived plasmid and assessed their effect on the growth of BW27783 strain and the FtsZ rings assembled by FtsZ55-56-SW-mNeonGreen at 37 ºC. Expression of EcFtsZ^{M225F} mildly affected the growth of *E. coli* BW27783 strain as compared to those expressing EcFtsZ (**Figure 6D, S4A**). Further, imaging and cell length calculations showed that the strain expressing EcFtsZ^{M225F} was almost 3-fold longer [average cell length of 11.73 µm ± 1.56 (number of cells counted were at least 226, N = 3)] than those expressing EcFtsZ [average length of 4.09 ± 0.81 µm (number of cells counted were at least 166, N = 3)]. These results further confirmed the division defects due to the expression of EcFtsZ^{M225F} (**Figure 6E**).

To test if the expression of EcFtsZ^{M225F} perturbed FtsZ ring assembly, we visualized the FtsZ rings assembled by the chromosomally encoded functional FtsZ$^{55-56}$-SW-mNeonGreen fusion protein under similar conditions. The untagged EcFtsZ^{M225F} was expressed from the plasmid (pJSB2-*EcFtsZ^{M225F}*) under the control of arabinose promoter

and induced with the addition of 0.2% arabinose at 37 ºC. As a control, the untagged EcFtsZ was expressed in a similar manner. Western blotting was performed to ascertain that both wildtype and the EcFtsZ^{M225F} were expressed at similar levels (**Figure S4B, C**). In cells expressing EcFtsZ, the Z-rings (visualized due to endogenous mNeonGreen tagged EcFtsZ) appeared as compact rings and were centrally located as expected. In contrast many of the cells expressing EcFtsZ^{M225F} were filamentous and contained multiple FtsZ rings or bands, which appeared uncompacted (**Figure 6F**). Next, we calculated the percentage of filamentous cells (defined as cells longer than 7 µm, (31)), of both wild type and M225F mutant in all the strains. The result showed higher percentage of cells (46.98 ± 2.84 for BW27783 at 37 ºC, and 48.54 ± 18.93 for JKD7_1 strain expressing mutant EcFtsZ^{M225F} at 42 ºC) with cell length above 7 µm than wild type. On the other hand, the wild type FtsZ expressing strains had a lower percentage of cells (i.e., 5.10 ± 3.92 for BW27783, and 10.56 ± 2.55 for JKD7_1 strain) longer than 7 µm (**Figure S4D**).

These results therefore suggest that the M225F mutation in EcFtsZ impairs the cell division of *E. coli* by affecting the Z-ring assembly and compaction of the ring.

Discussion

There are two structurally different states of FtsZ that help in its cooperative assembly into single protofilaments - R (monomer) and T (filament) states (23, 32, 33). FtsZ is known to treadmill at the site of division wherein one end polymerizes and the other end depolymerizes (11, 12). The difference in the rate of assembly and disassembly between two ends of filaments, the basis for which is unknown, defines the kinetic polarity. Our results provide a structural basis for GTP-dependent polymerization preferentially to one end of the single protofilament and, hence, for the kinetic polarity exhibited by FtsZ filaments. The directionality of growth proposed by us is the same as the observations from the earlier study on FtsZ polarity (26). We now provide the molecular basis for the directional growth.

Based on the crystal structures, we propose that the Gly71 peptide bond of the T3 loop is oriented to accommodate the gamma phosphate of GTP, in the GTP-bound (equivalent of GMPPNP) T-state. This conformational change enables hydrogen bonding between the gamma phosphate and the amide group of Gly71 (**Figure S2C**). The loop is disordered when GDP is present, probably due to the missing interactions with the T3 loop. This is consistent with previous reports, which state that GTP binding stabilizes the T3 loop of FtsZ (28, 34, 35). The flipping of the peptide favors the interaction with the next subunit as seen in the filament structure of FtsZ from *S. aureus* (**Figure S2C**; (35)) as well as the inferences from the DNP NMR study of GTP bound FtsZ filaments of *E. coli* (36). Our structures represent conformations of the T3 loop captured in the same crystal packing environment with a disordered T3 conformation in the GDP-bound T-state and a preference for a flipped Gly71 peptide in the GMPPNP-bound T-state. Both the T-state conformations of the loop are disordered compared to the well-ordered T3 loop conformation in chain A. The observation of a flipped peptide state of the T3 loop in response to GMPPNP-binding demonstrates that GMPPNP (or GTP) binding stabilizes the favorable conformation of T3 loop that assists in polymerization. We propose that the peptide flip and the stabilization of T3 loop conformation are key steps that determine the switch to a polymerization-competent monomer in the presence of GTP rather than GDP.

A similar observation was seen in tubulin structures where GTP binding activates tubulin for microtubule assembly (27). It was seen that upon binding of GTP molecule to tubulin, the T3 loop moves in order to accommodate the tri-phosphate. This in turn destabilizes the T5 loop, which causes the T3-T5 conflict and results in a conformational change in the T5 loop. This conformation of the T5 loop interacts with the incoming heterodimer (37). Thus, the feature of conformational changes upon GTP binding and interaction with the next subunit is conserved across corresponding regions of the tubulin fold in both FtsZ and tubulin. A communication between T3 and T5 loops occurs in other FtsZ structures too as observed from the hydrogen bond between Gln144 and the conserved proline backbone in T3 loop (PDB ID: 3WGN; **Figure S2D**). A similar interaction involving Tyr145 and Pro74, though with unclear density, is observed in our structure of SmFtsZ bound to GDP or GMPPNP in T-state (PDB ID: 7YOP, 7YSZ; chain

B) (**Figure 4C, D**). This, we think, is probably a characteristic feature of the T-state conformation of the NTD of FtsZ. Communication between T3 and T5 loops has also been proposed for tubulin (37).

Furthermore, it is observed from our structures that the NTD is in T-state nucleotide orientation whereas the cleft remains in the R-state orientation. This is referred to as an intermediate state or T/R state. The intermediate state captures a conformation in which only NTD with bound GMPPNP (GTP equivalent state) has been stabilized in the T-state. In an FtsZ filament, the T-state of NTD will be further stabilized by interactions with the adjacent subunit within the filament. This could occur independent of the conformational changes in CTD. It is interesting to note that an intermediate state where the CTD in T-state while H7 helix and NTD are in R-state is probably not possible because of incompatibility due to steric clashes at the interdomain cleft.

As the NTD transition from R- to T- state is independent of the CTD transition and GTP binding facilitates subunit interactions, GTP-bound FtsZ monomers could, in principle, attach to the bottom interface of the filament via the NTD, which is in T-state (**Figure S5**). Upon attaching to the bottom of the filament, the top interface interactions could further trigger the opening of the inter-domain cleft. We observe that the cleft mutant, SmFtsZ^{F224M} has higher GTPase activity than that of wild type. We infer that the mutation eases the transition of R- to T-state by facile opening of the cleft (**Figure S5**). The residue is located at the hinge where the inter-domain cleft opens and a flexible residue (Met224) in place of a rigid bulky residue (Phe224) might act as a lubricant for easier transition between states. The slower cleft opening in wild type SmFtsZ, therefore, could explain the lower GTPase activity of wild type SmFtsZ than that of EcFtsZ under identical *in vitro* conditions. The longer length of SmFtsZ^{F224M} filament might be accounted for by the lower critical concentration (CC), despite the higher GTPase activity. A similar effect is observed upon comparing SmFtsZ^{WT} and EcFtsZ, where SmFtsZ^{WT} filaments are shorter despite the higher GTPase activity in EcFtsZ. This might be attributed to the higher rate of addition to the filament when the CC is lower (nucleation rate = 1/CC), while the GTP binding affinity and rate of GTP hydrolysis at

the active site remain the same (38). In the *in vivo* study, when EcFtsZ-Met225 is mutated to phenylalanine, we observe filamentous morphology of cells indicative of aberrant cell division, due to perturbation of FtsZ assembly. It is likely that the slow R to T transition due to the bulky side chain of phenylalanine in the cleft affects the rate of subunit addition at the bottom end of the FtsZ filament.

It is possible that there is an inherent tendency for the NTD and CTD to go into an extended conformation if addition of subsequent monomers does not stabilize the T-state conformation. The extended conformation is not stable and thereby interacts with another monomer in extended conformation to form a domain-swapped dimer, as observed in crystal structures of wild type SmFtsZ and non-polymerizing mutants of other FtsZs too (PDB IDs: 1W5F, 5MN7; (23, 39)). In our crystal structures, the polymerization incompatible domain-swapped dimers of SmFtsZ preferentially crystallized compared to the globular monomers which tend to polymerize. The presence of strong contacts by means of a phenylalanine residue at the inter-domain cleft of SmFtsZ could act as a barrier for a smooth transition to the T-state. SmFtsZ monomer might have a higher propensity compared to EcFtsZ to go through an extended conformation during conversion from R-state to T-state. Previous reports have indeed shown that the NTD and the CTD are independent of each other, which can reconstitute non-covalently to form functional FtsZ (39), similar to a domain-swapped globular arrangement of NTD and CTD.

Our observations highlight the parallels in the polymerization mechanism of tubulin and FtsZ. In contrast to FtsZ, tubulin is composed of a heterodimer, which polymerizes to form microtubules (2). It is interesting to speculate that the existence of tubulin as a heterodimer has probably evolved to prevent a non-productive extended conformation of the NTD and CTD of the tubulin fold.

Materials and methods

Cloning

ftsZ genes from *S. melliferum* (UniProt ID: A0A037UPJ1) and *E. coli* (Uniprot ID: P0A9A6) were amplified from the genomic DNA of the respective organisms (*S. melliferum*: genomic DNA obtained from DSMZ, Germany, catalogue number 21833; *E. coli*: genomic DNA extraction from lab strain). In *Spiroplasmas*, the codon TGA codes for tryptophan whereas in *E. coli*, TGA is a stop codon. Therefore, for using *E. coli* as the heterologous expression system, all TGA codons in the *ftsZ* gene were changed to TGG (the codon which codes for tryptophan in *E. coli*). *ftsZ* gene from *S. melliferum* has two tryptophans which are coded by TGA, at the amino acid positions 384 and 411. These two tryptophan codons were changed to *E. coli* codon (TGG) using primers for site-directed mutagenesis. The genes were cloned into pHis17 vector (obtained from Löwe lab, MRC LMB, Cambridge; refer Addgene plasmid #78201 for vector backbone) using restriction-free cloning (40) between *NdeI* and *BamHI* restriction enzyme sites. The truncated constructs and the single-point mutants were also generated using PCR followed by *DpnI* digestion, transformation and screening for the positive clones using sequencing. The EcFtsZ mutant M225F was created using restriction-free cloning in pJSB100 (pBAD18Cm-EcFtsZ) by using respective primers (29). The list of primers used for cloning of the above genes and list of strains used in this study are given in **Tables S5 and S6**.

Protein purification

The plasmids were transformed into *E. coli* BL21(AI) cells and 1 L culture was grown in LB medium supplemented with ampicillin. The cultures were induced with 0.2 % (w/v) L-arabinose when its optical density (OD) at 600 nm reached 0.6 and was further incubated at 30 °C for 5 hours post-induction and cell harvested by spinning at 6000 *xg* at 4 °C. The pellet was resuspended with lysis buffer (50 mM Tris, pH 8, 200 mM NaCl and 10% glycerol) and sonicated. The lysate was centrifuged at 100,000 *xg* at 4 °C and the supernatant was loaded onto a 5 mL His-Trap (GE Lifesciences) column pre-equilibrated with buffer A (50 mM Tris, pH 8, 200 mM NaCl). The protein was eluted with a step gradient of imidazole containing buffer B (50 mM Tris, pH 8, 200 mM NaCl, 500 mM imidazole). The purest fractions of the protein were identified using 12 % SDS-PAGE

gel, pooled, concentrated and injected into the gel filtration column, Superdex 200 10/300 (GE Lifesciences), pre-equilibrated with the final buffer (HK50- 50 mM HEPES, pH 6.5, 50 mM KCl). The protein eluted at volumes corresponding to monomeric (major peak) and dimeric (small hump) size for SmFtsZ constructs. The fractions were pooled, concentrated, flash-frozen in aliquots, and stored at -80 °C till further use. The same protocol was followed for all other constructs of FtsZs. For wild type EcFtsZ, only affinity chromatography was carried out because size exclusion run gave a spread peak from the void till the monomeric size, indicating a heterogenous oligomeric state of the protein. The final proteins were visualized in SDS-PAGE gel to check for the purity (**Figure S1A**). The molecular weights of the purified protein was confirmed using mass spectrometry, since some of the constructs were observed to run aberrantly with respect to molecular weight markers on an SDS-PAGE gel.

Pelleting assay

Protein was spun at 100,000 *xg* at 4 °C in order to remove any precipitate. 10 μM of the protein was taken from the supernatant to set up 50 μL of reaction. The following reaction conditions were prepared- a) only protein, b) protein and $MgCl_2$, c) protein, $MgCl_2$ and GDP, and d) protein, $MgCl_2$ and GTP. A final concentration of 3 mM of nucleotide and 5 mM of $MgCl_2$ was taken for the reactions. The reaction mixtures were incubated at 30 °C for 10 minutes, spun at 100,000 *xg* at 30 °C for 15 minutes. The supernatant was taken out and the pellet was resuspended with buffer as equal volume of the reaction. The supernatant and pellet fractions were mixed with 2x Laemmli buffer and loaded onto 12 % SDS-PAGE gel in equal amounts.

Malachite green assay for estimating GTPase activity

The GTPase activity of all constructs was performed using Malachite green assay which is a colorimetric assay and measures the release of inorganic phosphate (41). The protein was spun at 22,000 *xg* at 4 °C and the reaction was set with the required concentration of protein, reaction buffer (50 mM HEPES, pH 6.5, 50 mM KCl), saturating concentration of GTP (obtained from Michaelis-Menten plot), and 5 mM $MgCl_2$. The reaction mixture

(20 μL) was incubated at 30°C for 15 minutes and stopped by addition of 10 mM of EDTA (5 μL). The reaction mixture was added to a 96 well plate and 100 μL of the malachite green mixture was added into the reaction mixture. Also, a set of phosphate standard solutions of known concentrations was prepared and added to the 96 well plate along with the malachite green mixture. After 10 minutes of incubation, absorbance was measured in Varioskan Flash (4.00.53) at 630 nm wavelength.

The concentration of phosphate released was calculated by dividing the slope obtained from the phosphate standard. The reaction containing buffer and only GTP was taken as blank and the absorbances were normalized by subtracting the blank. The Michaelis-Menten plots were generated with the y-axis as the rate of reaction that is phosphate released per unit time (μM/min) and the x-axis as different concentrations of GTP from 0-2.5 mM for EcFtsZ and 0-10 mM for SmFtsZ. The curve was fitted with the Michaelis Menten equation, $V_0 = V_{max}$ ([S]/([S] + K_M).

The k_{obs} (min^{-1}) of the proteins were calculated by dividing the concentration of phosphate released by time and the concentration of the protein and k_{cat} (min^{-1}) was determined by the formula $V_{max}/[E_t]$ from the Michaelis-Menten plot. The critical concentrations of the proteins were determined by obtaining the k_{obs} (min^{-1}) of different concentrations of the protein ranging from 0 to 10 μM for EcFtsZ and 0 to 14 μM for SmFtsZ. Statistical analysis was done with one-way ANOVA test and the statistical significance values were obtained using Tukey's multiple comparisons test. All the statistical analysis and plotting was done using version 9.00 for MacOS of GraphPad Software (San Diego California USA). Mean and standard error of mean (SEM) were calculated.

The value of the specific activity of EcFtsZ was comparable with the previously reported value (18, 22, 42), but higher than the values reported by other studies (7, 12, 43–45). The differences in the values of the specific activity of EcFtsZ might be due to differences in purification protocol, method for determining phosphate release, reaction buffer, and temperature.

Size exclusion chromatography (SEC) and Size exclusion chromatography with multi-angle light scattering (SEC-MALS)

For SEC-MALS, 100 µL of 2 mg/mL SmFtsZ$^{\Delta CT}$ was injected in GE superdex 200^{TM} column equilibrated with HK50 buffer (50 mM HEPES, pH 6.5, 50 mM KCl). The apparatus was connected to Wyatt Heleos II 18° angle light scattering which is coupled to a Wyatt Optilab rEX online refractive index detector. The data analysis was done using the ASTRA software 6.1.7.17 and the molar mass of the injected protein was calculated from the differential refractive index and the light scatter.

For SEC, 100 µL of 10 mg/mL SmFtsZ$^{\Delta CT}$ was injected in GE superdex 200^{TM} column equilibrated with HK50 buffer. The data was plotted in 9.00 for MacOS, GraphPad Software.

HPLC run to determine the nucleotide bound to the protein

50 mM of SmFtsZ$^{\Delta CT}$ was denatured at 75 °C, spun at 21,000 *xg* at 4 °C and the supernatant was filtered using 0.22 µm cellulose acetate filter (Corning). The filtrate was loaded onto DNAPAC PA 200 ion exchange column which was pre- equilibrated by buffer A (2 mM Tris, pH 8). The runs were performed using a linear gradient of 0 – 20 % buffer B (2 mM Tris, pH 8, and 1.25 M NaCl) for 3 column volumes (CV), 20 – 40 % buffer B for 3 CV and 100 % buffer B for 2 CV. The standards used for the run were GDP and GTP of 100 mM each. The graph was plotted with absorbance at 255 nm against the conductivity using version 9.00 for MacOS, GraphPad Software.

Crystallization of SmFtsZ$^{\Delta CT}$ with and without nucleotide addition

SmFtsZ$^{\Delta CT}$ crystallization was set up using around 500 commercially available screens (Molecular dimensions, Hampton Research) having 100 nL of 10 mg/mL protein and 100 nL of the respective condition in 96 well sitting drop plates where drop A had only protein with the condition and drop B had protein, GMPPNP, $MgCl_2$, and conditions. The initial hits obtained were optimized in order to get well diffracting crystals. Needle-like

crystals were obtained in the conditions tabulated in **Table S7**. The crystals were frozen with 20 % (v/v) ethylene glycol as cryoprotectant in the parent condition.

Structure determination

The crystals were diffracted and the final data collected at synchrotron sources at Diamond Light Source (Harwell, UK) and ELETTRA (Trieste, Italy). The diffraction data was indexed using XDS and scaled using AIMLESS present in the CCP4i package (46, 47). Molecular replacement was done with BsFtsZ structure (PDB ID: 2VXY) using PHASER and model building was done using COOT (48, 49). Refinement was done using PHENIX (50). The data collection and refinement statistics are tabulated in **Tables S3** and **S7**.

Transmission electron microscopy

Transmission electron microscopy was carried out to visualize the filaments of the wild-type SmFtsZ and SmFtsZ^{F224M}. The protein was spun at 100,000 *xg* at 4 °C and a reaction of 20 μL was set with a final protein concentration of 10 μM and GTP concentration of 3 mM at 30 °C for 15 minutes. Another set of samples was prepared by resuspending the pellet obtained after 100,000 *xg* spin for 15 minutes at 30 °C of the aforementioned reaction, with the same volume of buffer as the reaction.

5 μL of protein was added on a glow discharged (one round of 15 mA current for 25 seconds using plasma cleaner, Quorum Technologies) carbon and formvar coated grid and incubated for 2 minutes before blotting out the protein. 5 μL of sterile MilliQ water was added and kept for 30 seconds and finally, 5 μL of 2 % (w/v) uranyl acetate was added and incubated for 30 seconds and blotted out. The grids were dried before imaging under TEM (JEM- 2200FS Joel Ltd.). The images of the filaments were analysed using ImageJ (51).

Sequence analysis

FtsZ sequence of *E. coli* (UniProt ID: P0A9A6) was used to acquire sequences using the EVfold webserver (52). The sequences with identity percentages ranging from 19 – 100

% were retrieved from UniProtKB. All significant hits except redundancies and low-quality sequences were selected and aligned with MUSCLE in JALVIEW (ver 2.11.4) (53). After generating the alignment, a 90 % redundancy cutoff was applied. The total number of sequences considered for the analysis was 818.

For acquiring only *Spiroplasma* FtsZ sequences, the FtsZ sequence from *S. melliferum* was used as a query sequence for BLAST against all *Spiroplasmas*. A total of 26 *Spiroplasma* FtsZ sequences were obtained.

Structural analysis

For the analysis of FtsZ structures (**Table S4**), representative structures for T-state and R-state were taken from SaFtsZ (PDB ID: 3WGN and 3VOA) and BsFtsZ (PDB ID: 2RHL). For the analysis of guanine angle, SaFtsZ T-state structure (PDB ID: 5H5G, Chain A) was taken as reference and the N-terminal domain was superimposed with other T- and R-state structures available at the Protein Data Bank (PDB). The angles were calculated by estimating the agle between the two axes drawn using the 'define axis' tool by selecting three atoms (C2, C8, N1) for each structure. The movement of CTD with respect to NTD was calculated by measuring the RMSD between the C-alpha of the reference structure and the sample structure. For all the superimpositions, the NTD of the molecules (residue number 1 to 170) was superimposed using 'matchmaker' command in Chimera. All the analyses are done using UCSF Chimera version 1.13.1 (54).

Growth and culturing of bacteria

E. coli strain *BW27783 (FtsZ 55-56 SW-mNeonGreen)* was grown in LB Lennox at 37 ºC. *E. coli* strain JKD7_1/ pKD3 (*repA*^{ts}) was grown in LB Lennox containing 25 μg/ mL Kanamycin and 100 μg/ mL carbenicillin at 30 ºC or at a restrictive temperature of 42 ºC to allow for the loss of pKD3 plasmid. The *ftsZ84* strain was grown in no salt LB medium at 30 ºC. Chloramphenicol, wherever necessary, was used at concentration of 34 μg/ mL. Expression of EcFtsZ and EcFtsZ^{M224F} from the plasmid pJSB100 was achieved by the addition of 0.2 % L-arabinose. Glucose at 1 % was used for repression.

Complementation Assay (Spot Assay)

Complementation assay was performed as previously described by Stricker et. al. (29). Briefly JKD7-1/pKD3 strain carrying pJSB2 or pJSB100 or pJSB2 derived plasmids was grown overnight in repression medium containing 1 % glucose at 30 °C. The overnight culture is serially diluted starting with OD_{600} 0.8 - 1.0 and then increasing dilution factor from 5^0 to 5^6. Three microliters of each dilution were spotted on repression plates containing 1 % glucose and induction plates containing 0.2 % L-arabinose using a 48-pin replicator (VP-Scientific). The plates containing 0.2 % L-arabinose were incubated at a restrictive temperature of 42 °C and repression plates containing 1 % glucose at 30 °C. BW27783 strain carrying pJSB2 or pJSB100 or pJSB2 derived plasmids was grown at 37 °C and similarly spotted in LB plates containing either 1 % glucose or 0.2 % L-arabinose.

Western Blot

Expression of FtsZ was detected by western blotting using anti-FtsZ antibodies (AS10715: Agrisera). BW27783 was grown as described above and cell lysates were subjected to SDS-PAGE, followed by western blotting. Briefly, 3 mL cultures were harvested by centrifugation at 2800 *xg* for 5 minutes, followed by 3 times wash with 1X PBS and resuspended in a 100-200 µL Laemmli buffer with 10-20 µL β-mercaptoethanol. The suspension was vortexed and left on ice for 5 minutes. The sample were then sonicated (40 % amplitude with 1 second on & 3 seconds off) for 3 - 4 cycles. The lysate was centrifuged at 10,000 *xg* for 2 minutes and supernatant was transferred into a fresh tube and 1.8 µL of Laemmli buffer was added and heated at 98 °C for 10 - 15 minutes, before loading the samples to 12 % SDS-PAGE gel. The proteins in the gel were transferred to a polyvinylidene difluoride membrane (Immobilon-P) using a semidry transfer apparatus (Amersham Life Sciences or Trans Blot Turbo Transfer System from Bio-Rad). Membranes were blocked using PBS containing 2% BSA and 0.05% Tween-20. Subsequently, anti-FtsZ antibody (AS10715: Agrisera) at a dilution of 1:10,000 was prepared in 1X PBS containing 2% BSA and 0.05% Tween-20 and incubated for 1.5 h at room temperature (RT). The blots were washed three times in PBST (0.05% Tween-20). Then Protein A-HRP at a dilution of 1:15,000 prepared in 1X PBS containing 2% BSA

and 0.05% Tween-20 was added and incubated for 1 hour at RT. The blot was subsequently washed 3-4 times with 20 mL of PBST (0.05% Tween-20). Final detection was carried out using chemiluminescence HRP substrates (Immobilon Western Chemiluminescent HRP Substrate; WPKLS0500; Merck Millipore) and imaged using ChemiDoc XRS+ (Bio-Rad).

Microscopy

The bacterial strains (JKD7-1/pKD3 with appropriate plasmids) were grown overnight in repression media at 30 °C and then sub-cultured by diluting 1:100 times into media containing 0.2 % L-arabinose. Growth was continued further at 42 °C by diluting 1:10 times at 1.5 hours intervals at least twice. The cultures were grown to an OD_{600} between 0.3 - 0.6 and 1.5 mL culture was centrifuged at 2800 x*g* for 3 minutes. The cell pellets were gently resuspended in 150 µL of fresh LB medium of which 1 – 2 µL were spotted on 1.7 % LB-agarose pads and imaged. Similarly, BW27783 strain was grown overnight at 37 °C, diluted 1:100 into fresh medium and imaged using agarose pads after 2 hours when they reached an OD_{600} of 0.4 – 0.6. The cells were imaged on agarose pads. LB-agarose pads were prepared with LB (Lennox) media containing 1.7 % agarose in cavity slides and covered with a coverslip No. 1.5 (VWRI631-0125). Images were acquired using an epifluorescence microscope (DeltaVision™ Elite) with a 100X oil immersion phase objective (PLN100XOPH) of NA 1.25 and an in-line CCD camera (CoolSNAP™ HQ2). An oil of refractive index 1.514 was used for imaging bacteria cells. A Spectra 7, Lumencor Light Engine© (solid-state illumination) was used as a light source with a 1 mm diameter liquid light guide. Excitation filters and emission filters of 488/28 nm and 525/48 nm respectively were used for imaging mNeonGreen tagged strains.

Author Contributions

JC designed and performed all the experiments, analyzed data other than those mentioned below and wrote the manuscript, SMP performed, analyzed and wrote the *in vivo* section, SD helped in cloning and purification of the SmFtsZ^{D211G} mutant and edited the manuscript, VB performed the sequence analysis and assisted with protein purification, SH assisted in standardization of purification and pelleting assays of EcFtsZ, RS supervised and wrote the *in vivo* work, PG conceptualized, supervised the project and wrote the manuscript.

Acknowledgments

Synchrotron facilities at Diamond Light Source, UK and ESRF, Grenoble [through ESRF Access Program of the Department of Biotechnology (Grant No. BT/INF/22/SP22660/2017)] and access to DST ELETTRA XRD2, Jyotsna from Dr. Radha Chauhan's lab at NCCS for access to the SEC-MALS facility at NCCS, Pune, macromolecular crystallography facility at IISER Pune, and electron microscopy facilities at the Advanced Technology Platform Centre, Regional Centre for Biotechnology, Faridabad, and at IISER Pune with support from DST under Nanomission program (EMR/2016/003553) are acknowledged. We thank Dr. Harold Erickson (Duke University, USA) and Dr. Kerwyn Casey Huang (Stanford University) for strains and plasmids. We acknowledge fellowships from IISER Pune to JC and SH, DAE to SMP, and CSIR to SD. Research work in the lab of PG was supported by Department of Biotechnology (DBT) Membrane Structural Biology Program grant (BT/PR28833/BRB/10/1705/2018), SERB CRG (CRG/2018/003795) and IISER Pune, and SERB (EMR/2016/000487), DBT (BT/PR15183/BRB/10/1443/2015, and BT/INF/22/SP33046/2019) and intramural core funding from Department of Atomic Energy (DAE) to RS.

References

1. K. J. Begg, W. D. Donachie, Cell shape and division in *Escherichia coli*: experiments with shape and division mutants. *J. Bacteriol.* **163**, 615–622 (1985).

2. E. Nogales, K. H. Downing, L. A. Amos, J. Löwe, Tubulin and FtsZ form a distinct family of GTPases. *Nat. Struct. Biol.* **5**, 451–458 (1998).

3. E. Bi, J. Lutkenhaus, FtsZ ring structure associated with division in *Escherichia coli*. *Nature* **354**, 161–164 (1991).

4. X. Ma, D. W. Ehrhardt, W. Margolin, Colocalization of cell division proteins FtsZ and FtsA to cytoskeletal structures in living *Escherichia coli* cells by using green fluorescent protein. *Proc. Natl. Acad. Sci.* **93**, 12998–13003 (1996).

5. C. A. Hale, P. A. J. de Boer, Direct Binding of FtsZ to ZipA, an essential component of the septal ring structure that mediates cell division in *E. coli*. *Cell* **88**, 175–185 (1997).

6. W. Margolin, FtsZ and the division of prokaryotic cells and organelles. *Nat. Rev. Mol. Cell Biol.* **6**, 862–871 (2005).

7. P. de Boer, R. Crossley, L. Rothfield, The essential bacterial cell-division protein FtsZ is a GTPase. *Nature* **359**, 254–256 (1992).

8. X. Wang, J. Lutkenhaus, The FtsZ protein of *Bacillus subtilis* is localized at the division site and has GTPase activity that is dependent upon FtsZ concentration. *Mol. Microbiol.* **9**, 435–442 (1993).

9. H. P. Erickson, Modeling the physics of FtsZ assembly and force generation. *Proc. Natl. Acad. Sci. U. S. A.* **106**, 9238–9243 (2009).

10. C. Coltharp, J. Buss, T. M. Plumer, J. Xiao, Defining the rate-limiting processes of bacterial cytokinesis. *Proc. Natl. Acad. Sci.* **113**, E1044–E1053 (2016).

11. A. W. Bisson-Filho, *et al.*, Treadmilling by FtsZ filaments drives peptidoglycan synthesis and bacterial cell division. *Science* **355**, 739–743 (2017).

12. X. Yang, *et al.*, GTPase activity–coupled treadmilling of the bacterial tubulin FtsZ organizes septal cell wall synthesis. *Science* **355**, 744–747 (2017).

13. J. M. Monteiro, *et al.*, Peptidoglycan synthesis drives an FtsZ-treadmilling-independent step of cytokinesis. *Nature* **554**, 528–532 (2018).

14. J. W. McCausland, *et al.*, Treadmilling FtsZ polymers drive the directional movement of sPG-synthesis enzymes via a Brownian ratchet mechanism. *Nat. Commun.* **12**, 609 (2021).

15. J. Löwe, L. A. Amos, Crystal structure of the bacterial cell-division protein FtsZ. *Nature* **391**, 203–206 (1998).

16. H. P. Erickson, FtsZ, a prokaryotic homolog of tubulin? *Cell* **80**, 367–370 (1995).

17. H. P. Erickson, D. W. Taylor, K. A. Taylor, D. Bramhill, Bacterial cell division protein FtsZ assembles into protofilament sheets and minirings, structural homologs of tubulin polymers. *Proc. Natl. Acad. Sci.* **93**, 519–523 (1996).

18. A. Mukherjee, Dynamic assembly of FtsZ regulated by GTP hydrolysis. *EMBO J.* **17**, 462–469 (1998).

19. S. Huecas, J. M. Andreu, Energetics of the cooperative assembly of cell division protein FtsZ and the nucleotide hydrolysis switch. *J. Biol. Chem.* **278**, 46146–46154 (2003).

20. S. Huecas, *et al.*, Energetics and geometry of FtsZ Polymers: Nucleated self-assembly of single protofilaments. *Biophys. J.* **94**, 1796–1806 (2008).

21. I. V. Surovtsev, J. J. Morgan, P. A. Lindahl, Kinetic modeling of the assembly, dynamic steady state, and contraction of the FtsZ Ring in prokaryotic cytokinesis. *PLOS Comput. Biol.* **4**, e1000102 (2008).

22. A. Dajkovic, A. Mukherjee, J. Lutkenhaus, Investigation of regulation of FtsZ assembly by SulA and development of a model for FtsZ polymerization. *J. Bacteriol.* **190**, 2513–2526 (2008).

23. J. M. Wagstaff, *et al.*, A polymerization-associated structural switch in FtsZ that enables treadmilling of model filaments. *mBio* **8** (2017).

24. J. Fujita, *et al.*, Identification of the key interactions in structural transition pathway of FtsZ from *Staphylococcus aureus*. *J. Struct. Biol.* **198**, 65–73 (2017).

25. L. C. Corbin, H. P. Erickson, A unified model for treadmilling and nucleation of single-stranded FtsZ protofilaments. *Biophys. J.* **119**, 792–805 (2020).

26. S. Du, S. Pichoff, K. Kruse, J. Lutkenhaus, FtsZ filaments have the opposite kinetic polarity of microtubules. *Proc. Natl. Acad. Sci.* **115**, 10768–10773 (2018).

27. M. Knossow, V. Campanacci, L. A. Khodja, B. Gigant, The mechanism of tubulin assembly into microtubules: Insights from structural studies. *iScience* **23**, 101511 (2020).

28. T. Yoshizawa, *et al.*, Crystal structures of the cell-division protein FtsZ from *Klebsiella pneumoniae* and *Escherichia coli*. *Acta Crystallogr. Sect. F* **76**, 86–93 (2020).

29. J. Stricker, H. P. Erickson, *In vivo* characterization of *Escherichia coli* ftsZ Mutants: Effects on Z-Ring structure and function. *J. Bacteriol.* **185**, 4796–4805 (2003).

30. D. A. Moore, Z. N. Whatley, C. P. Joshi, M. Osawa, H. P. Erickson, Probing for binding regions of the FtsZ protein surface through site-directed insertions:

Discovery of fully functional FtsZ-fluorescent proteins. *J. Bacteriol.* **199**, e00553-16 (2016).

31. D. P. Haeusser, V. W. Rowlett, W. Margolin, A mutation in *Escherichia coli* ftsZ bypasses the requirement for the essential division gene zipA and confers resistance to FtsZ assembly inhibitors by stabilizing protofilament bundling. *Mol. Microbiol.* **97**, 988–1005 (2015).

32. M. R. Caplan, H. P. Erickson, Apparent cooperative assembly of the bacterial cell division protein FtsZ demonstrated by isothermal titration calorimetry. *J. Biol. Chem.* **278**, 13784–13788 (2003).

33. T. Matsui, *et al.*, Structural reorganization of the bacterial cell-division protein FtsZ from *Staphylococcus aureus*. *Acta Crystallogr. D Biol. Crystallogr.* **68**, 1175–1188 (2012).

34. J. F. Díaz, *et al.*, Activation of Cell Division Protein FtsZ: Control of switch loop T3 conformation by the nucleotide γ-phosphate*. *J. Biol. Chem.* **276**, 17307–17315 (2001).

35. F. M. Ruiz, *et al.*, FtsZ filament structures in different nucleotide states reveal the mechanism of assembly dynamics. *PLOS Biol.* **20**, e3001497 (2022).

36. K. M. McCoy, A. E. McDermott, GTP-bound *E. coli* FtsZ filaments are composed of tense monomers: A DNP NMR study using interface detection. *bioRxiv*, 2022.04.01.486622 (2022).

37. A. Nawrotek, M. Knossow, B. Gigant, The determinants that govern microtubule assembly from the atomic structure of GTP-tubulin. *J. Mol. Biol.* **412**, 35–42 (2011).

38. K. Jain, *et al.*, Polymerization kinetics of tubulin from mung seedlings modeled as a competition between nucleation and GTP-hydrolysis rates. *Cytoskeleton* **78**, 436–447 (2021).

39. M. A. Oliva, S. C. Cordell, J. Löwe, Structural insights into FtsZ protofilament formation. *Nat. Struct. Mol. Biol.* **11**, 1243–1250 (2004).

40. F. van den Ent, J. Löwe, RF cloning: A restriction-free method for inserting target genes into plasmids. *J. Biochem. Biophys. Methods* **67**, 67–74 (2006).

41. J. Feng, *et al.*, An improved malachite green assay of phosphate: mechanism and application. *Anal. Biochem.* **409**, 144–149 (2011).

42. T. Mohammadi, *et al.*, The GTPase Activity of *Escherichia coli* FtsZ Determines the Magnitude of the FtsZ Polymer Bundling by ZapA *in Vitro*. *Biochemistry* **48**, 11056–11066 (2009).

43. A. Mukherjee, K. Dai, J. Lutkenhaus, *Escherichia coli* cell division protein FtsZ is a guanine nucleotide binding protein. *Proc. Natl. Acad. Sci.* **90**, 1053–1057 (1993).

44. K. Dai, A. Mukherjee, Y. Xu, J. Lutkenhaus, Mutations in ftsZ that confer resistance to SulA affect the interaction of FtsZ with GTP. *J. Bacteriol.* **176**, 130–136 (1994).

45. X. Wang, J. Huang, A. Mukherjee, C. Cao, J. Lutkenhaus, Analysis of the interaction of FtsZ with itself, GTP, and FtsA. *J. Bacteriol.* **179**, 5551–5559 (1997).

46. P. R. Evans, G. N. Murshudov, How good are my data and what is the resolution? *Acta Crystallogr. D Biol. Crystallogr.* **69**, 1204–1214 (2013).

47. L. Potterton, *et al.*, *CCP* 4 *i* 2: the new graphical user interface to the *CCP* 4 program suite. *Acta Crystallogr. Sect. Struct. Biol.* **74**, 68–84 (2018).

48. A. J. McCoy, *et al.*, Phaser crystallographic software. *J. Appl. Crystallogr.* **40**, 658–674 (2007).

49. P. Emsley, B. Lohkamp, W. G. Scott, K. Cowtan, Features and development of *Coot*. *Acta Crystallogr. D Biol. Crystallogr.* **66**, 486–501 (2010).

50. P. D. Adams, *et al.*, *PHENIX*: a comprehensive Python-based system for macromolecular structure solution. *Acta Crystallogr. D Biol. Crystallogr.* **66**, 213–221 (2010).

51. C. A. Schneider, W. S. Rasband, K. W. Eliceiri, NIH Image to ImageJ: 25 years of image analysis. *Nat. Methods* **9**, 671–675 (2012).

52. T. A. Hopf, *et al.*, The EVcouplings Python framework for coevolutionary sequence analysis. *Bioinformatics* **35**, 1582–1584 (2019).

53. A. M. Waterhouse, J. B. Procter, D. M. A. Martin, M. Clamp, G. J. Barton, Jalview Version 2—a multiple sequence alignment editor and analysis workbench. *Bioinformatics* **25**, 1189–1191 (2009).

54. E. F. Pettersen, *et al.*, UCSF Chimera—A visualization system for exploratory research and analysis. *J. Comput. Chem.* **25**, 1605–1612 (2004).

Figures:

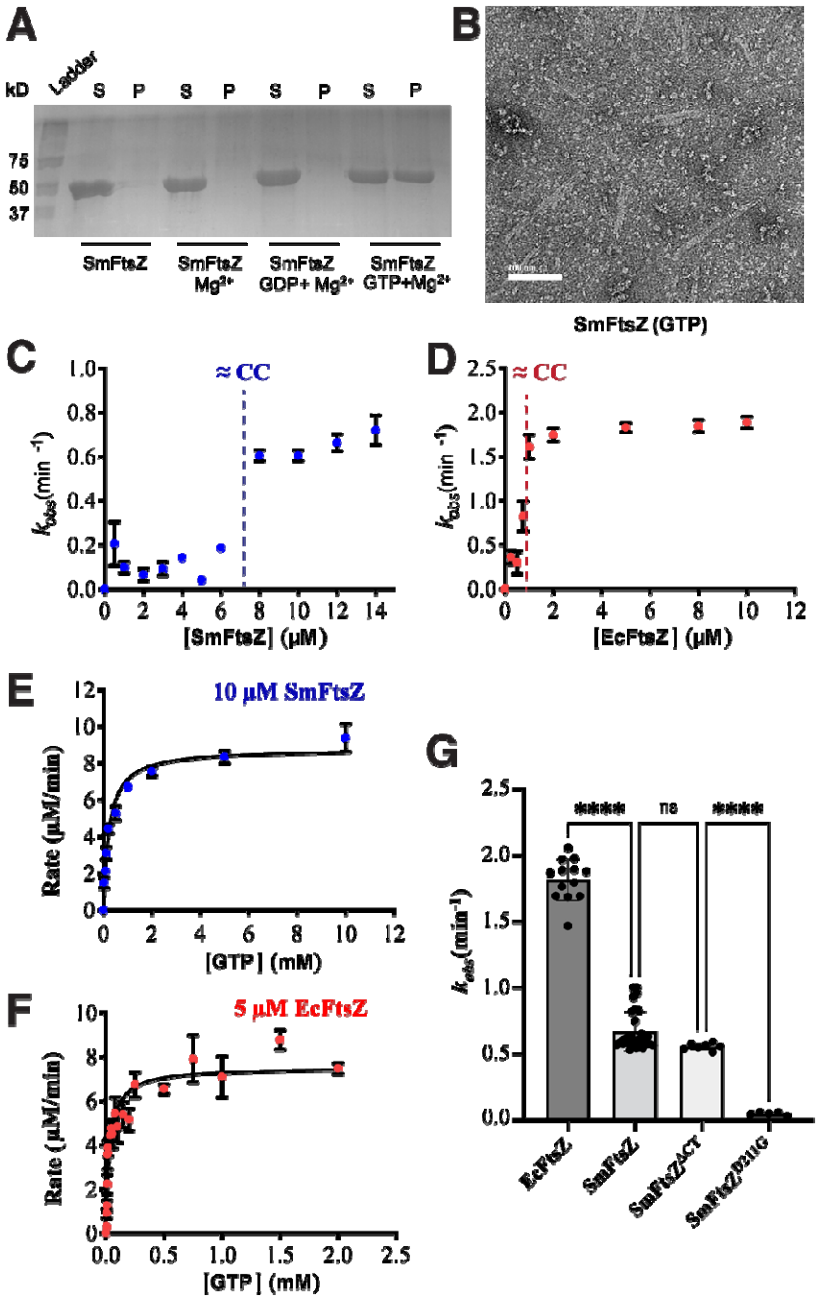

Figure 1. Critical concentration required for SmFtsZ filament formation is higher while its GTPase activity is slow as compared to EcFtsZ.

A) A representative 12 % SDS-PAGE gel showing pelleting assay of SmFtsZ to determine the condition necessary for SmFtsZ filament formation. Incubation of SmFtsZ (10 µM) in presence of (i) Mg^{2+} (10 mM), (ii) Mg^{2+} (10 mM) and GDP (3 Mm) and (iii) Mg^{2+} (10 mM) and GTP (3 mM) followed spinning at 100,000 *xg* revealed that the protein pelleted only in the last condition. The presence of SmFtsZ in the pellet suggested that it formed filaments. S and P represents fraction in supernatant and pellet of the reaction. B) Visualization of the SmFtsZ (10 µM) pellet obtained in presence of Mg^{2+} (10 mM) and GTP (3 mM), using transmission electron microscope confirmed presence of protein filaments. Scale bar represents 100 nm. C) and D) GTPase activity of SmFtsZ and EcFtsZ was measured with different concentrations of the protein, respectively (SmFtsZ [WT; N = 3; n = 4], EcFtsZ [WT; N = 3; n = 3]. E) GTPase activity of SmFtsZ was measured with different concentrations of GTP ranging from 0 to 10,000 µM (blue). The curve was fitted with Michaelis-Menten equation, $V_0 = V_{max}$ ([S]/([S] + K_M). (N = 3; n= 3). F) GTPase activity of EcFtsZ was measured with different concentrations of GTP ranging from 0 to 2000 µM (red) (N = 3; n = 3). G) Comparison of k_{obs} of FtsZs from both the organisms. $SmFtsZ^{D211G}$, a GTPase dead mutant, was taken as negative control. The experiments were done with saturating concentration of GTP (2.5 mM for SmFtsZ and 1 mM for EcFtsZ). (EcFtsZ [N = 4; n= 5], SmFtsZ [N = 3; n = 20], $SmFtsZ^{\Delta CT}$ [N = 2; n = 7], and $SmFtsZ^{D211G}$ [N = 1; n = 5]; N = number of independent purification batches and n = number of repeats). The mean with SEM and 95% confidence intervals is shown in the long and short horizontal lines in panel F, one-way ANOVA; ****p < 0.0001; ns, non-significant. The estimated k_{obs} values are tabulated in **Table S2**.

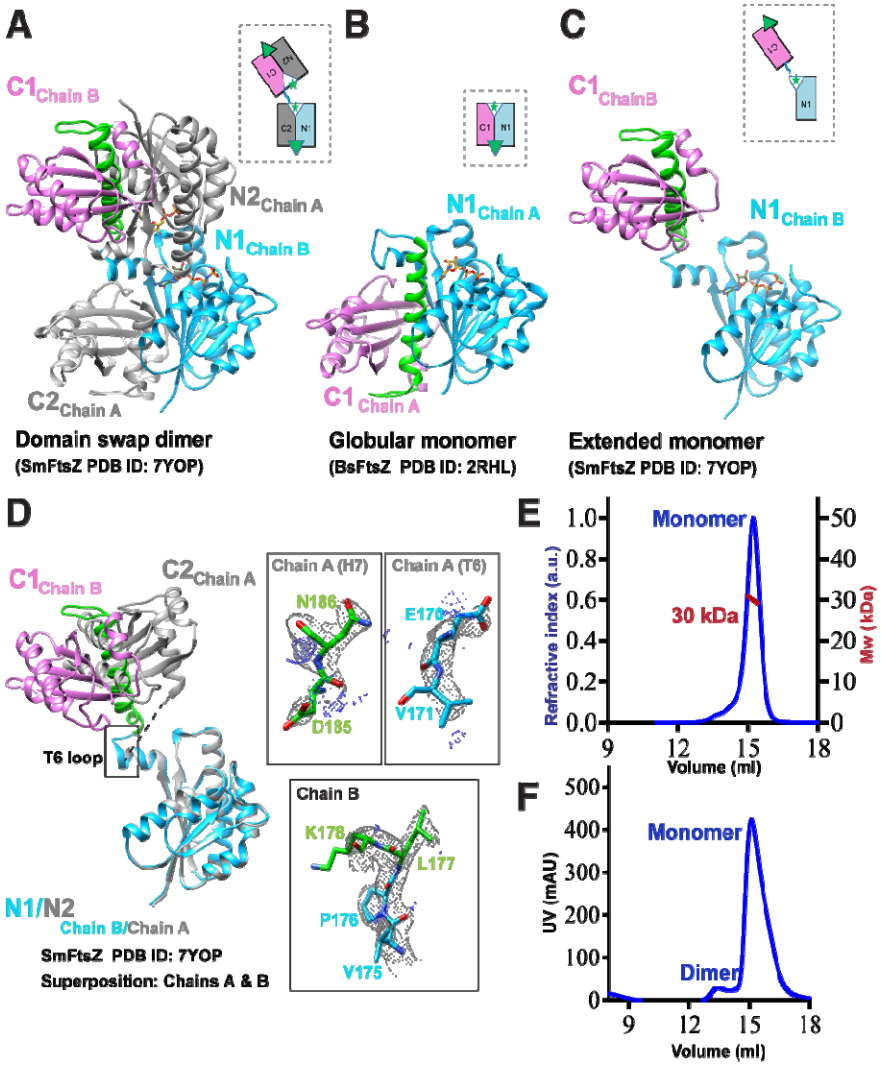

Figure 2. SmFtsZ crystallized as a domain-swap dimer.

A) Overall structure of SmFtsZ, along with the schematic containing both the chains forming domain-swap dimers. The domains and the chains are denoted with the respective color; PDB ID: 7YOP. B) Overall structure of globular FtsZ from *B. subtilis* (PDB ID: 2RHL). C) Overall structure of monomer of SmFtsZ (PDB ID: 7YOP, chain B). D) Relative orientations of the CTD in the extended conformation of each chain, fixing C- alpha of NTD of both the chains. Electron density map of the region shown in the inset where the two domains separate at T6 loop (map $F_o - F_c$ shown at 2.5 σ, blue and $2F_o - F_c$ at 1.2 σ, black). E) SEC-MALS chromatogram of SmFtsZ $^{\Delta CT}$. SmFtsZ$^{\Delta CT}$ loaded at 100 µL of 2 mg/mL (low concentration) (protein concentration on the column is

around > 1/10th of the concentration loaded). The profile shows a single monodisperse peak with average molecular mass at 30 kDa. F) SEC profile of SmFtsZ$^{\Delta CT}$ at 100 µL of 10 mg/mL (high concentration) shows two peaks: one major peak at 15 mL (monomer) and another small hump at 13.5 mL (dimer).

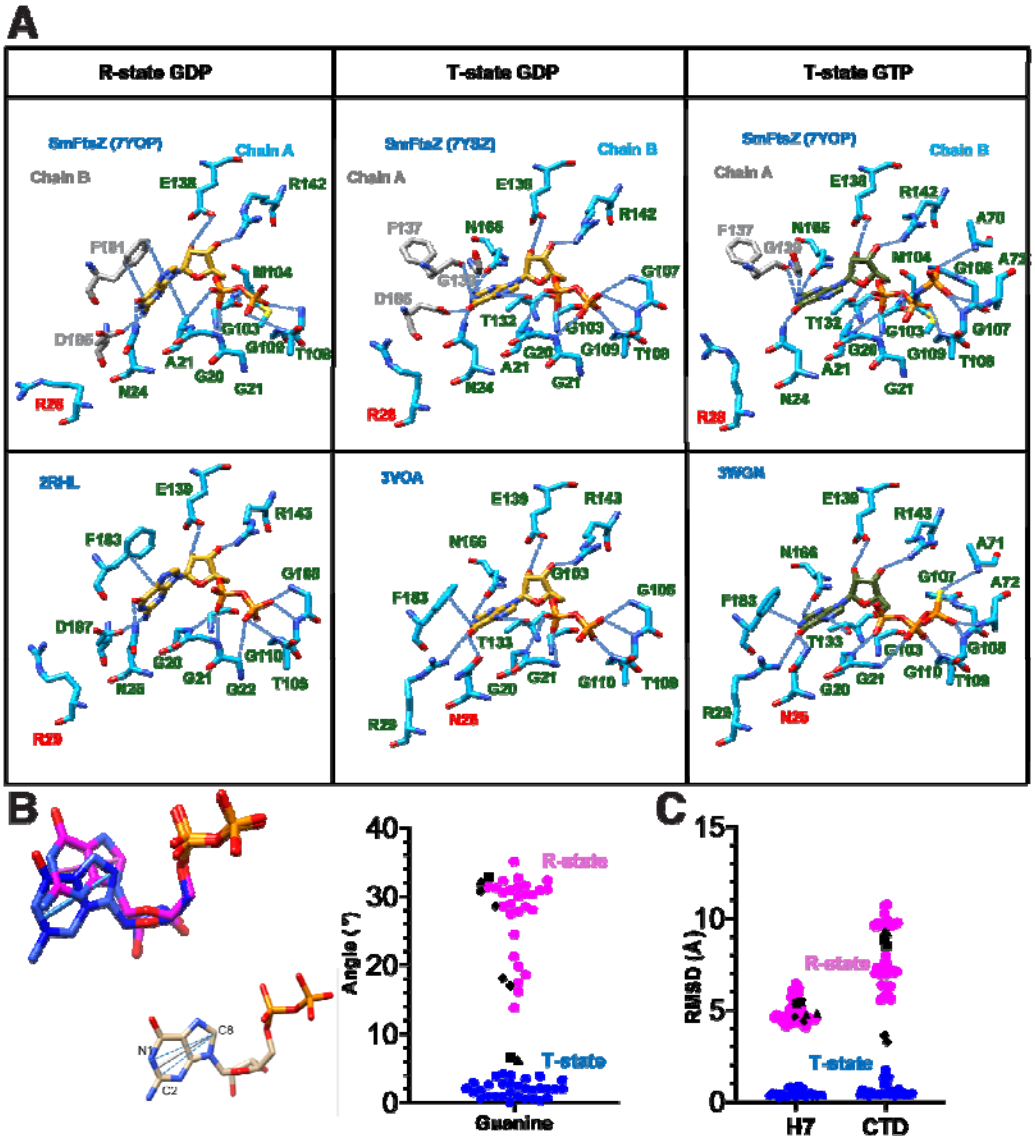

Figure 3. SmFtsZ structure shows R and T states in the NTD and R state in the CTD.

A) Nucleotide conformation of BsFtsZ in R-state in GDP (2RHL), SaFtsZ in T state in GDP (3VOA), GTP (3WGN) along with that of SmFtsZ are shown (GDP- brown, GTP- olive green). B) Quantification of the guanine ring tilt angle keeping a T state structure (PDB ID- 5H5G) as reference. Inset shows atoms selected (C2, C8, N1) for guanine/nucleotide angle calculation. C) Quantification of the CTD movement, keeping T state structure (PDB ID- 5H5G) as reference. The pink cluster shows the structures in R

state and the blue cluster shows the structures in T state. Black triangle represents both the chains of PDB ID: 7YOP (SmFtsZ) and black square represents PDB ID: 7YSZ (SmFtsZ). The black diamonds represent the other reported domain-swapped dimers (PDB ID: 1W5F and 5MN7). Both the domain-swapped structures are considered in the graph plotted in (B). For the graph in (C), both the chains of PDB ID: 1W5F is only taken because PDB ID: 5MN7 does not form a globular organization of NTD and CTD in the domain-swapped dimer.

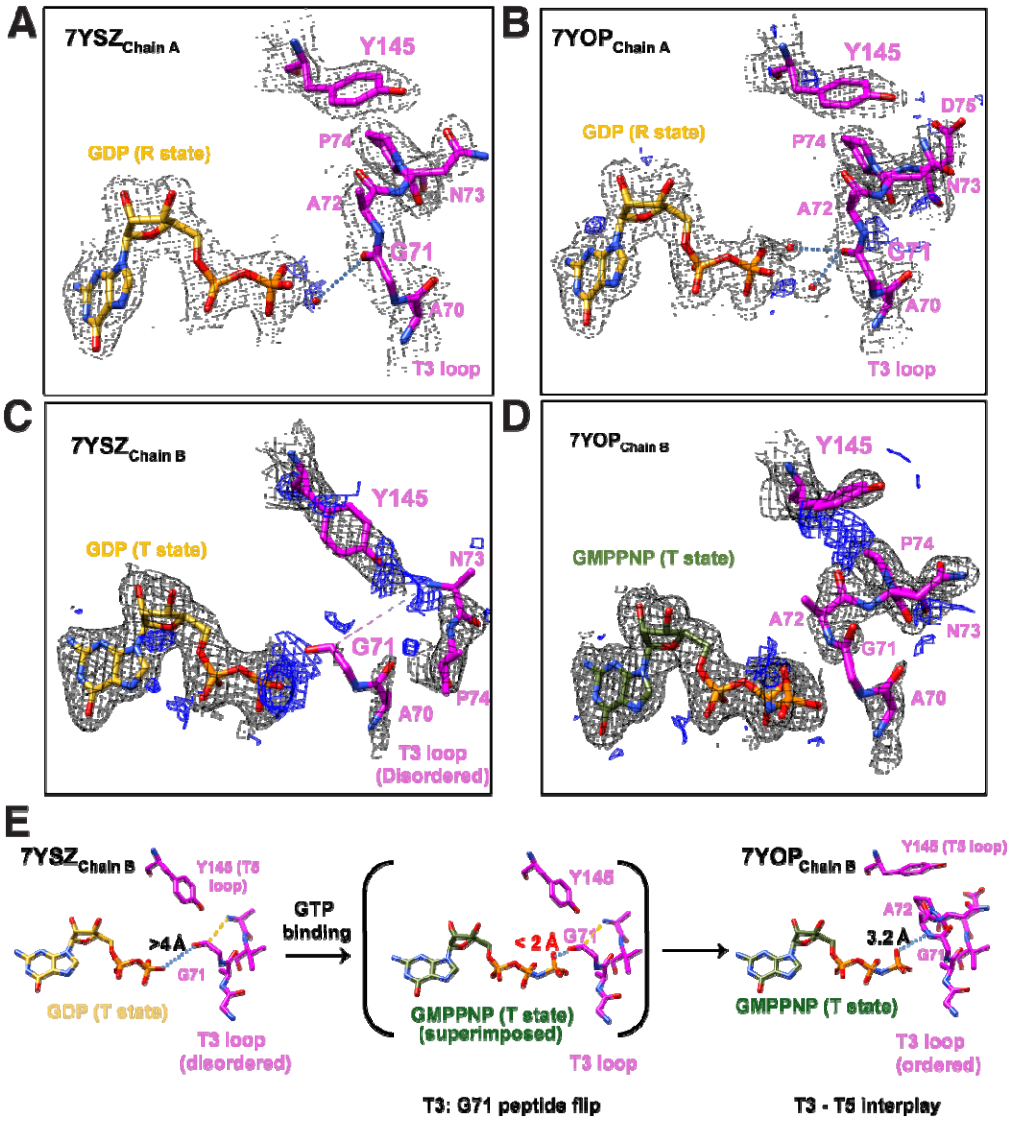

Figure 4. Filament compatible conformation of T3 loop is stabilized by Gamma-phosphate of the nucleotide

A), B) Electron density map for the orientation of T3 loop in R state GDP-bound structure of SmFtsZ (PDB ID: 7YSZ, chain A; PDB ID: 7YOP, chain A, respectively). C), D) Electron density map for the orientation of T3 loop in T state GDP and GMPPNP structure of SmFtsZ (PDB ID: 7YSZ, chain B; PDB ID: 7YOP, chain B, respectively), Map $F_o - F_c$ shown at 2.5 σ (blue) and $2F_o - F_c$ at 1.2 σ (black). E) Comparison of SmFtsZ structure bound to GDP (chain B, PDB ID: 7YSZ) and SmFtsZ bound to

GMPPNP (chain B, PDB ID: 7YOP). The carboxyl group of G71 of T3 loop faces towards the nucleotide pocket. The loop is disordered in the presence of GDP in T state. The GMPPNP binding induces T3 conflict due to which the Gly71 peptide of T3 loop flips.

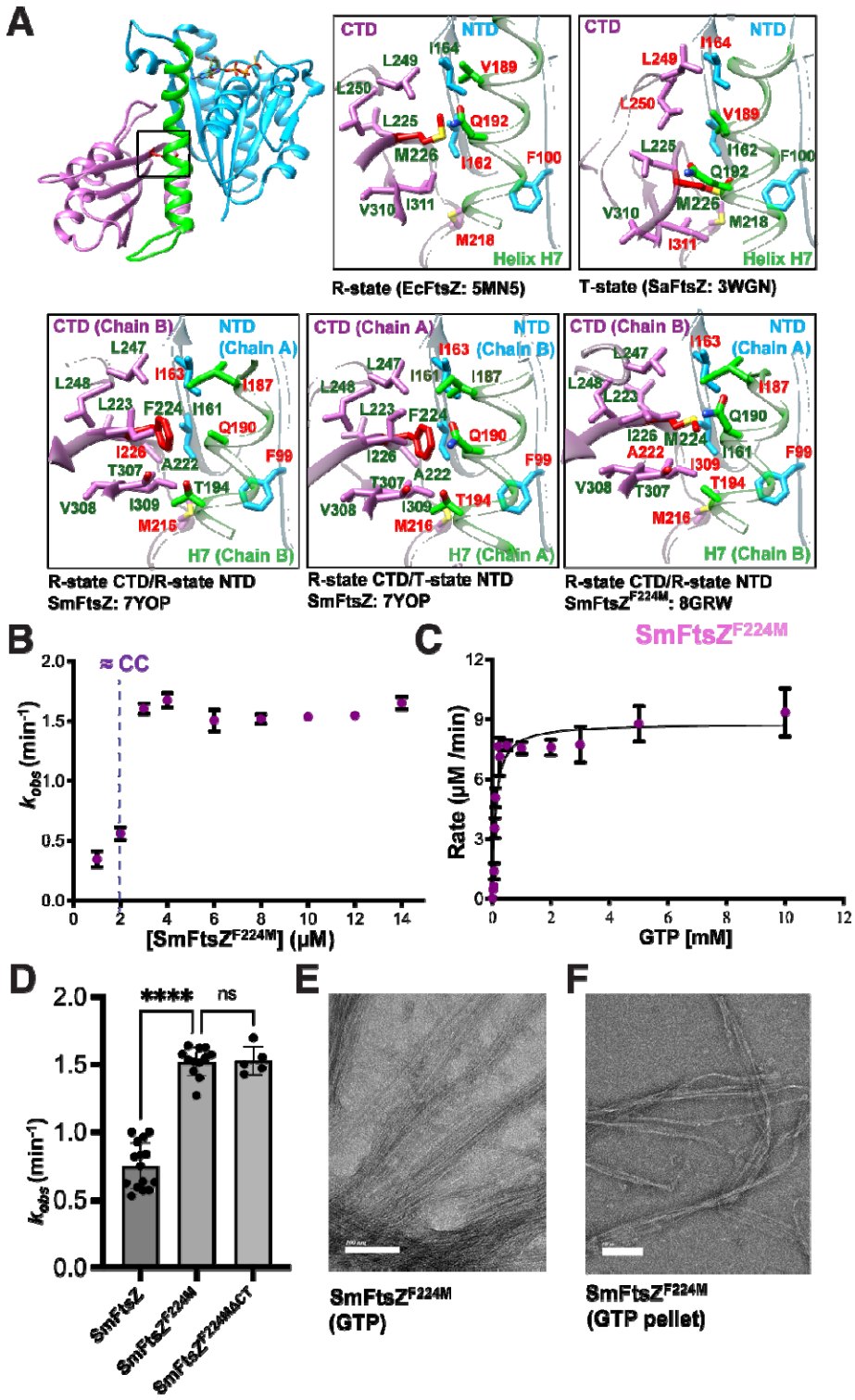

Figure 5. Hyperactive mutant of SmFtsZ plays role in the ease of transition of state.

A) Overall structure of FtsZ (PDB ID: 3WGN), the boxes highlight the position of the methionine, the residue of interest. The insets show the position of M226 in SaFtsZ and SmFtsZ in S7 strand comparing R-state (SaFtsZ; PDB ID: 5MN5), T-state (SaFtsZ; PDB ID: 3WGN), chain A and chain B of SmFtsZ (PDB ID: 7YOP), and chain A of $SmFtsZ^{F224M}$ (PDB ID: 8GRW) highlighting the movement of the CTD. B) GTPase activity of $SmFtsZ^{F224M}$ was measured with different concentrations of the protein ranging from 0 to 14 µM, [N = 2; n = 4]. C) GTPase activity of $SmFtsZ^{F224M}$ was measured with different concentrations of GTP ranging from 0 to 10,000 µM (purple). The curve was fitted with Michaelis-Menten equation, $V_0 = V_{max}$ ([S]/([S] + K_M), [N = 2; n = 3]. D) GTPase activity comparison of $SmFtsZ^{F224M}$ mutant with the wild type construct ($SmFtsZ^{F224M}$ [N = 2; n = 12], $SmFtsZ^{F224M\Delta CT}$ [N = 2; n = 5] and SmFtsZ [N = 3; n = 15]). The mean with SEM and 95% confidence intervals is shown in the long and short horizontal lines in panel F, one-way ANOVA; ****p < 0.0001; ns, non-significant. E) TEM image of $SmFtsZ^{F224M}$ with 10 µM protein and 3 mM GTP. Scale bar represents 100 nm. F) TEM image of $SmFtsZ^{F224M}$ with 10 µM of protein and 3 mM GTP after 100,000 *xg* spin, resuspending the pellet in the same volume of buffer as the total volume of reaction. The experiments were done with saturating concentration of GTP. Scale bar represents 100 nm.

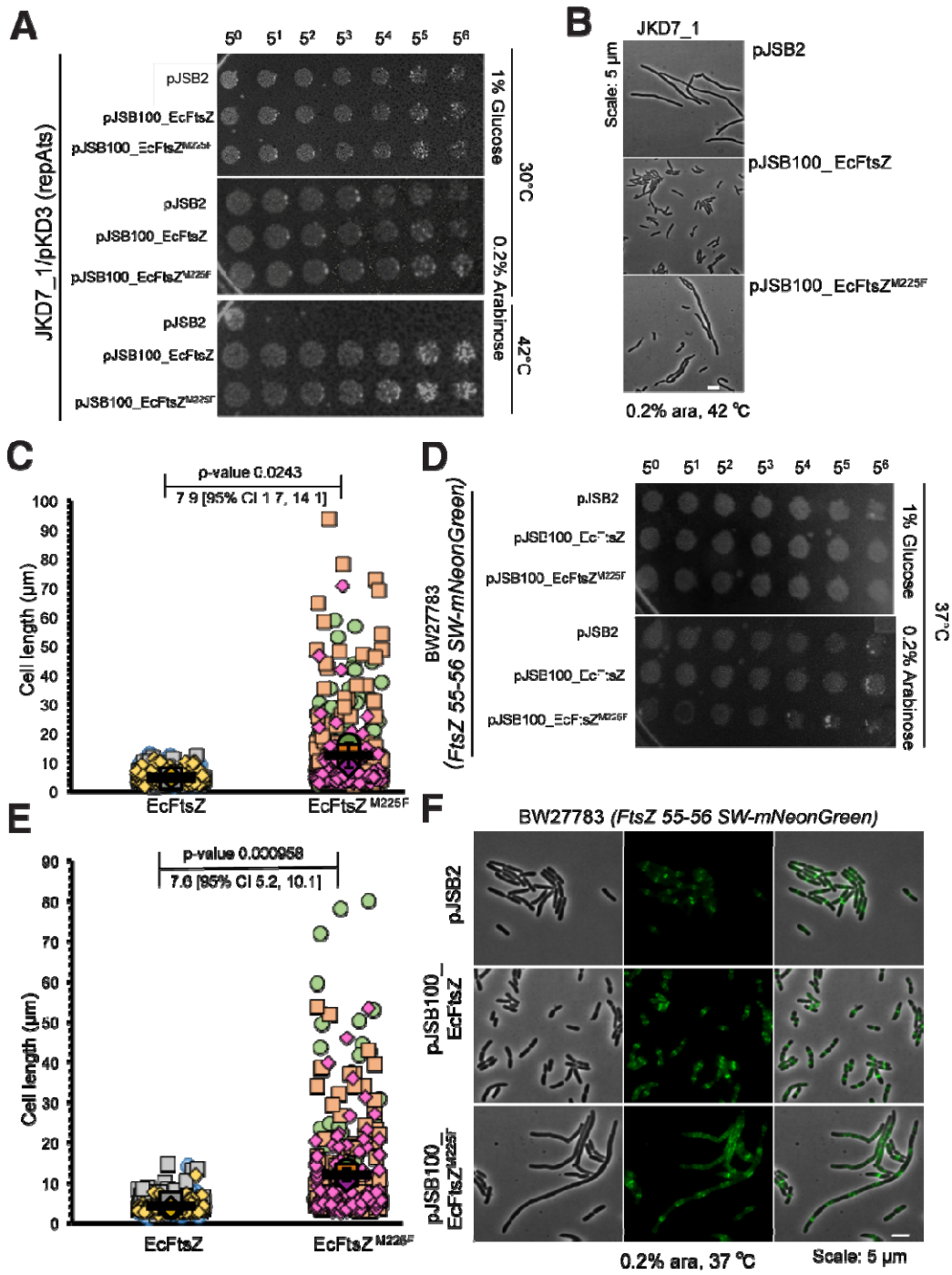

Figure 6. M225F mutation in EcFtsZ impairs *E. coli* growth and cell division.

A) JKD7_1/ pKD3 strain carrying pJSB2 (vector) or pJSB100 (EcFtsZ) or pJSB100-EcFtsZ^{M225F} plasmids were spotted on the repressible plate (1 % glucose) or inducible

plate (0.2 % L-arabinose). The plates containing L-arabinose were incubated at either permissible (30 °C) or non-permissible (42 °C) temperatures. Each subsequent spot was five times serially diluted. B) The cell morphology of the JKD7_1 strain carrying pJSB2 (vector) or pJSB100 (EcFtsZ) or pJSB100-EcFtsZ^{M225F} plasmids were observed by phase-contrast imaging after 6 hours of growth at 42 °C, when the pKD3 plasmid is lost and expression of FtsZ is solely from the pJSB plasmids. C) The wildtype EcFtsZ expressing JKD7_1 strain had an average cell length of 4.58 µm ± 0.09 (number cells counted were at least 218, N=3) and the cells expressing mutant EcFtsZ^{M225F} were 12.45 µm ± 4.47 (number of cells counted were at least 100, N=3) long. The quantitative data are shown as super plots and P-values and effect size are indicated above the plots. D) BW27783 strains with pJSB100 plasmids were also spotted on the repressible and inducible plates at 37 °C with five times of serial dilution. E) Cultures of BW27783 strain were grown at 37 °C in presence of 0.2 % L- arabinose until they reached an OD_{600} of 0.4 - 0.6 and imaged by phase-contrast microscopy. The quantitative data of the cell length for EcFtsZ and EcFtsZ^{M225F} expressing in BW27783 are shown as super plots. Expression of the mutant EcFtsZ^{M225F} resulted in an average cell length of 11.73 µm ± 1.56 (number of cells counted were at least 226, N=3), as compared to those expressing wildtype EcFtsZ, which had an average length of 4.09 µm ± 0.81 (number of cells counted were at least 166, N=3). P-values and effect size are indicated above the plots. F) FtsZ rings were imaged in BW27783 strain (FtsZ 55-56-mNeonGreen-SW) carrying empty vector (pJSB2) or ectopically expressing EcFtsZ or EcFtsZ^{M225F} by epifluorescence microscopy. Ectopic expression of EcFtsZ^{M225F} resulted in aberrant FtsZ ring compaction and cell division. Scale bar = 5 µm. Statistical significance was assessed by paired two-tailed Student's *t* test. P values were calculated using microsoft excel formula T-TEST. The error bars shown are inferential and represent 95% confidence interval (CI).